

Defect Passivation Using a Phosphonic Acid Surface Modifier for Efficient RP Perovskite Blue-Light-Emitting Diodes

Jayanta Kumar Mishra, Natalia Yantara,* Anil Kanwat, Tomoki Furuhashi, Sankaran Ramesh, Teddy Salim, Nur Fadilah Jamaludin, Benny Febriansyah, Zi En Ooi, Subodh Mhaisalkar, Tze Chien Sum, Kedar Hippalgaonkar, and Nripan Mathews*



Cite This: <https://doi.org/10.1021/acsmi.2c00899>



Read Online

ACCESS |



Metrics & More



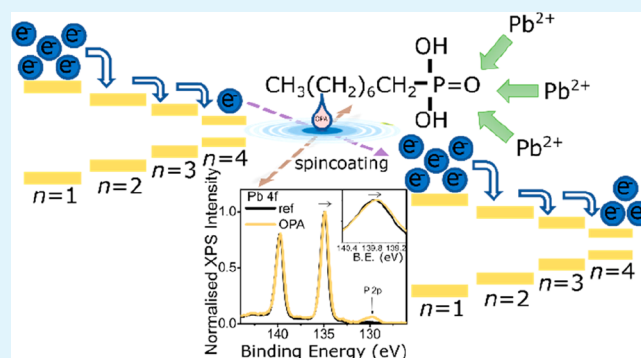
Article Recommendations



Supporting Information

ABSTRACT: Defect management strategies are vital techniques for enhancing the performance of perovskite-based optoelectronic devices, such as perovskite-based light-emitting diodes (Pe-LEDs). As additives can act as both crystallization modifier and/or defect passivator, a thorough study on the roles of additives is essential, especially for blue emissive Pe-LEDs, where the emission is strictly controlled by the n -domain distribution of the Ruddlesden–Popper (RP, $L_2A_{n-1}Pb_nX_{3n+1}$, where L is bulky cations, A is monovalent cations, and X is halide anions) perovskite films. Among several additives, octyl phosphonic acid (OPA) is of interest because of its ability to bind with uncoordinated Pb^{2+} (a notorious nonradiative defects site) and therefore passivates them. Here, with the help of X-ray photon-spectroscopy (XPS), Fourier-transform infrared spectroscopy (FTIR), and photoluminescence quantum yield (PLQY) measurements, we demonstrated the capability of OPA to bind and passivate unpaired Pb^{2+} defect sites. Crystallization modification to enhance higher n -domains can also be observed from steady-state and transient absorption (TA) measurements. Upon OPA treatment, both efforts enhanced the PLQY and the external quantum efficiency (EQE) of PeLED up to 53% and 3.7% at 485 nm, respectively.

KEYWORDS: halide perovskites, light emitting diode, crystallization modulator, Ruddlesden–Popper perovskite, quasi 2D perovskite



INTRODUCTION

Halide perovskites (HP) with a crystal structure of ABX_3 , where A is a monovalent cation (methylammonium (MA^+), formamidinium (FA^+), and cesium (Cs^+)), B is a divalent metal cation (Pb^{2+} and Sn^{2+}), and X is a halide anion (I^- , Br^- , and Cl^-), have emerged over the past decade for use as next-generation semiconductors.^{1,2} HPs have been demonstrated for use in a wide range of applications because of their bandgap tunability,³ narrow photoluminescence line width,^{4,5} high photoluminescence quantum yield (PLQY),⁶ long minority carrier diffusion length ($>1 \mu m$),^{7–9} high defect tolerance, and solution processability. After the first report on perovskite-based LED (PeLED) (EQE $< 1\%$) in 2014, tremendous progress has been achieved to this date with record external quantum efficiencies (EQEs) of PeLEDs beyond 20%^{10,11} for both green and red emissive PeLEDs. On the other hand, blue-emissive PeLEDs lag far behind, as they face many challenges such as high nonradiative recombination centers due to the presence of defects and electroluminescence spectral instability due to halide ion migration and phase segregation in the perovskite.¹² Despite the high defect tolerance of HPs, surface and grain boundary defects in thin films play a critical role in charge-carrier transport and nonradiative recombination,

which lowers the PLQY, efficiency, and stability of the PeLEDs. During the crystallization of these solution-processed HP films, their surfaces can terminate with PbX_2 or AX or both, leading to a change in the electronic band structure of the surface and bulk.¹³ The type of surface termination using surface modifiers and external stimuli, i.e., moisture and light, can further significantly influence the band alignment. Thus, understanding the type of defects and developing effective passivation strategies are crucial for achieving stable and high-performance devices. Numerous passivating strategies have been introduced to eliminate these defects, especially uncoordinated Pb^{2+} or halide vacancies. Alkali metal oxide, i.e., Na^+ , K^+ , and Rb^+ ions, have been shown to reduce ion migration by passivating the halide vacancies.^{14–17} Lewis base additives such as triphenylphosphine oxide (TPPO), and 61

Special Issue: Novel Trends in Halide Perovskites for Optoelectronic Applications

Received: January 15, 2022

Accepted: April 27, 2022

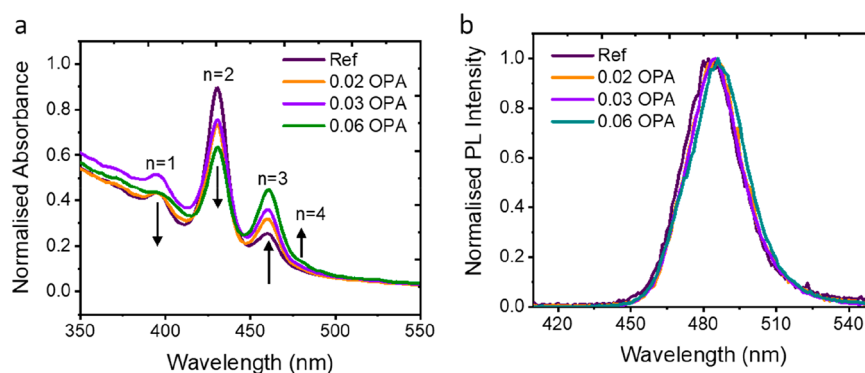


Figure 1. (a) Absorption spectra and (b) photoluminescence spectra of control and OPA-treated samples.

trioctylphosphine oxide (TOPO)₂ have been shown to act as surface modifiers by binding with the uncoordinated Pb²⁺ on the surfaces.^{18,19} Organic molecules have also been examined for passivating the uncoordinated Pb²⁺ defects using functional groups such as C–O, P–O, and –NH₂.^{19–24}

Interestingly, our recent study that uses additives such as TPPO, TOPO, pyridine, and *tert*-butylpyridine (TBP)²⁵ eliminated their role as passivating agents. Instead, they act as crystallization and phase distribution modulators as demonstrated using a PBA₂Cs_{*n*–1}Pb_{*n*}Br_{3*n*+1} mixed dimensional structure, where PBA (4-phenyl-1-butylammonium) acts as a bulky organic cation in between *n*-domains consisting of lead halide octahedral layers (1, 2, 3, 4, ..., ∞) in the Ruddlesden–Popper (RP) phase. The study suggests that the electrochromic luminescence (EL) efficiency enhancement in the devices using additives is due to the formation of higher *n*-domains with higher Br content. RP perovskites primarily use ammonium (NH₃⁺) functional groups for defect passivation to form a mixed dimensional structure. The bulky functional group fits in between two-dimensional (2D) slabs of multiple thicknesses, also called *n*-domains, promoting charge carrier funneling from thin (lower *n*-domains with higher bandgap) to thick (higher *n*-domain with lower bandgap) slabs. Therefore, the proper distribution of *n*-domains is critical to retain high radiative recombination in the emitting domains through energy funneling.^{26,27} Although additives have been advantageous in surface or bulk defect passivation, their effect on RP perovskites is elusive. Moreover, the use of different additives other than the functional group (L) (a typical RP structure consisting of L₂A_{*n*–1}Pb_{*n*}X_{3*n*+1}), whether it modulates *n*-domain distribution or passivates surface defects by binding with uncoordinated Pb²⁺ or hydrogen bond (H-bond) interaction with Br, has yet to be fully understood. This is especially important for blue-emissive PeLEDs using monohalide RP perovskites, where stringent control over *n*-domain distribution is needed.

The coordination of organic ligands with metallic Pb can be better understood using the principles of coordination chemistry for the synthesis of HP nanocrystals. The softer, anionic, Lewis base ligands that target uncoordinated Pb²⁺ have been shown to produce absolute quantum yields.^{28,29} In phosphonic acid ligand group, octyl phosphonic acid (OPA, C₈H₁₉O₃P) that contains P–O and P=O has been shown to fall in that category and has produced unity PLQY.^{30–36} Thus, the role of such ligands to passivate defects in a mixed halide perovskite is crucial, which is yet to be examined.

Herein, we investigate the use of octyl phosphonic acid in blue emissive RP (PBA₂Cs_{*n*–1}Pb_{*n*}Br_{3*n*+1}) perovskites to

passivate the uncoordinated Pb²⁺ on the surface.^{30–36} Simultaneously, we show the effect of OPA as a crystallization modulator on PBA₂Cs_{*n*–1}Pb_{*n*}Br_{3*n*+1} RP perovskites. We further demonstrate that the OPA-treated PBA₂Cs_{*n*–1}Pb_{*n*}Br_{3*n*+1} films result in PLQY as high as 50% using a combined strategy, surface modifier, and phase modulator, which improved 3.7% EQE enhancement at an emission wavelength of 485 nm.

EXPERIMENTAL SECTION

Perovskite Precursor Preparation. The perovskite compounds PbBr₂ and CsBr were commercially purchased from TCI and sigma Aldrich. 4-Phenyl-1-butylammonium bromide salt (PBABr, C₆H₅(CH₂)₄NH₃Br) was synthesized by reacting 4-phenyl-1-butylamine with hydro-bromic acid at 0 °C under continuous argon flow. The perovskite precursors were prepared by mixing 2 M PbBr₂ and 2 M PBABr and 0.25 M CsBr. The first two precursors (PbBr₂ and PBABr) were made with the solvent 75%:25% DMF and DMSO and the third precursor (CsBr) was made with only DMSO. All the precursors PbBr₂, PBABr, and CsBr₂ was then mixed with a ratio of (1:1.3:5.33) to get the final precursor 0.2 M. Perovskite thin films were prepared by spin coating perovskite precursors with antisolvents being introduced halfway during spin coating. Although toluene was used as the antisolvent of the control samples, OPA with different concentrations was added to the toluene and used as the antisolvent for OPA-treated samples. The volumes of both the perovskite precursors and the antisolvent employed during coating were kept constant for all samples. The thin film samples were then encapsulated with UV-cured epoxy and taken out of glovebox for further optical measurements (i.e., absorbance, transient absorbance, transient photoluminescence). Similarly, for light-emitting device fabrication instead of glass substrate, an ITO-coated glass substrate was used.

Device Fabrication. The pre-etched ITO (indium tin oxide) on the glass substrate was washed in ultrasonication with the following solutions subsequently: detergent (Docomo) solution (5% detergent with DI water), DI water, isopropyl alcohol, and acetone. The substrates were then dried by an argon gun and treated for 30 min by UV ozone. The hole transport layer, poly(3,4-ethylenedioxythiophene) polystyrenesulfonate (PEDOT:PSS) was filtered (0.25 μm) and spin-coated onto the glass/ITO substrate at 4000 rpm for 60 s. It was then thermally annealed at 200 degrees for 40 s to remove any residual solvents. Afterward, the substrates were taken inside the glovebox with an argon atmosphere. The perovskite precursor was then spin-coated at 5000 rpm for 30 s inside the glovebox. Toluene or OPA added toluene was used as an antisolvent, which drop-casted onto the perovskite after 6 s of the beginning of spin coating of perovskite to induce fast nucleation. Thereafter, the organic electron transport layer (ETL) ((1,3,5-triazine-2,4,6-triyl)tris(benzene-3,1-diyl))tris(diphenylphosphine oxide) (PO-T2T) of 45 nm thick was evaporated onto it, followed by metal (LiF (1 nm)/Al (100 nm)) deposition to complete the device.

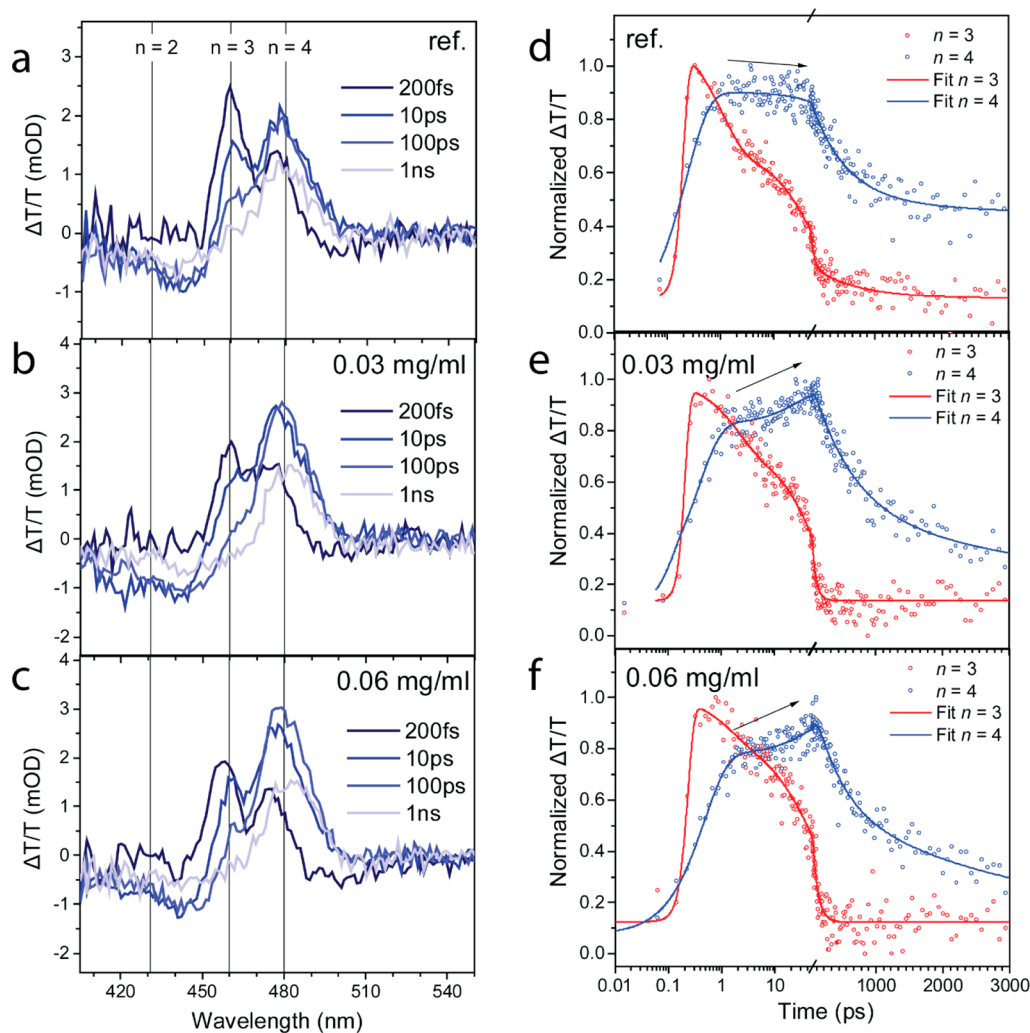


Figure 2. Transient absorption spectra of $\text{PBA}_2\text{Cs}_{n-1}\text{Pb}_n\text{Br}_{3n+1}$ films prepared with (a) blank toluene (ref), (b) 0.03 OPA, and (c) 0.06 OPA as antisolvent. The charge carriers kinetics of $n = 3$ and $n = 4$ domains are plotted for films prepared with (d) toluene (ref), (e) 0.03 OPA, and (f) 0.06 OPA as antisolvent. Upward and downward slopes of the trajectory indicate an increase and decrease in charge carrier funneling, respectively. Black vertical lines represent $n = 2, 3$, and 4 domains. The black arrows in the plots represent the dynamics that show (d) decay for the reference and (e, f) growth for the treated samples. The samples were excited at ~ 400 nm at a fluence of $4.4 \mu\text{J}/\text{cm}^2$ and probed with a white light continuum.

160 ■ RESULTS AND DISCUSSION

161 The effect of OPA treatment on $\text{PBA}_2\text{Cs}_{n-1}\text{Pb}_n\text{Br}_{3n+1}$ system
 162 was studied by varying the concentration of OPA solutions
 163 (i.e., 0.02, 0.03, and 0.06 mg/mL in toluene, which are labeled
 164 as 0.02, 0.03, and 0.06 OPA, respectively). From the
 165 absorption spectra (Figure 1a), the existence of RP perovskites
 166 with multiple n -domains were detected on control samples
 167 (ref), for which at least three excitonic peaks (at 396, 431, and
 168 461 nm) were observed. These excitonic peaks were assigned
 169 to the excitonic features of RP perovskites with $n = 1, 2$, and 3 ,
 170 respectively, with increasing wavelength.^{2,37,38} In addition, a
 171 shoulder at ~ 480 nm was observed on steady-state absorbance
 172 that can be attributed to the features of the $n = 4$ RP domain.
 173 Here, the $n = 1, 2$, and 3 excitonic absorption features were
 174 observed as sharp peaks, whereas a broader peak/signal was
 175 observed for $n = 4$, probably due to the decreasing binding
 176 energy with increasing n value.³⁹ Upon OPA treatment, the
 177 intensity of the excitonic feature of $n = 2$ was reduced, whereas
 178 that of $n = 3$ and $n = 4$ were amplified with increasing OPA
 179 concentration. Although features of multiple n -domains were

observed from absorption spectra, single photoluminescence 180
 (PL) peaks were observed for all samples (Figure 1b). The 181
 discrepancy here could be ascribed to the efficient energy 182
 transfer from low n -domains to high n -domains upon 183
 photoexcitation.^{37,38} Despite the changes in the absorbance 184
 features, similar PL peak positions were observed after OPA 185
 treatment. Although the main PL peaks were similar, the 186
 parasitic PL peaks at lower wavelengths, which correspond to 187
 the lower n -domains, were reduced upon OPA treatment 188
 (Figure S1). PL mapping of the films indicates that OPA 189
 treatment does not change the uniformity of the samples 190
 (Figure S2). Hence, the reduction in lower n -domains and the 191
 enhancement in higher n -domains featured in absorbance and 192
 PL spectra indicates the growth of RP perovskite n -domains 193
 upon OPA treatment. 194

To dive deeper into the n -domain distribution of the 195
 $\text{PBA}_2\text{Cs}_{n-1}\text{Pb}_n\text{Br}_{3n+1}$ films without and with OPA treatment, 196
 we employed transient absorption (TA) spectroscopy. The 197
 details of the experimental setup are given in the Experimental 198
 Section. An excitation wavelength of 400 nm and a low pump- 199

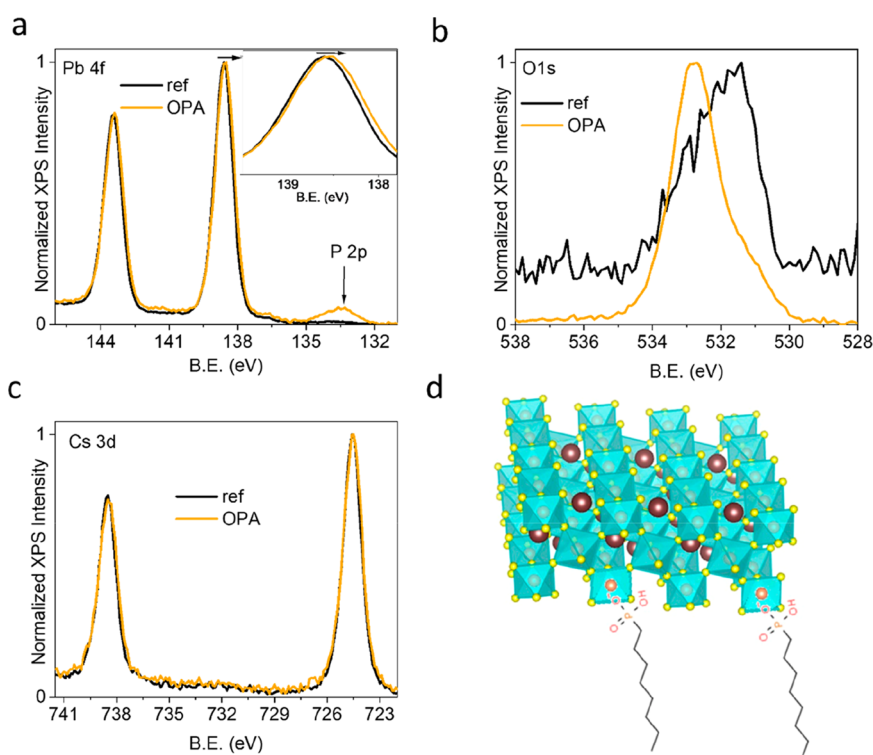


Figure 3. Binding energy spectra of $\text{PBA}_2\text{Cs}_{n-1}\text{Pb}_n\text{Br}_{3n+1}$ films prepared by using toluene (ref) and 0.03 OPA as antisolvent. The blown out spectra of (a) Pb 4f and P 2p, (b) O 1s, and (c) Cs 3d together with (d) the proposed schematic diagram of OPA interaction with the uncoordinated Pb^{2+} at the surfaces.

fluence of $4.4 \mu\text{J}/\text{cm}^2$ was employed to minimize Auger effects. Figure 2a–c shows the slices of the TA spectra for the reference and 0.03 and 0.06 OPA-treated samples, respectively. In all the samples, multiple photobleaching (PB) peaks ranging from 430 to 480 nm (assigned as $n = 2$, $n = 3$, and $n = 4$ domains, respectively) were observed. First, the TA spectrum at an early delay time (200 fs) was considered to reflect the phase distribution in the film, as it precedes the energy transfer process. The observed relative intensity of phases is in agreement with the steady-state absorption measurement. The OPA treatment modulates the n -domain distribution in the treated films compared to the reference, which is evident from the higher relative intensity of the $n = 4$ n -domain in the OPA-treated samples (Figure 2b, c) compared to the reference samples (Figure 2a) at the early pump–probe delay. Hence OPA treatment reduces the formation of lower n -domains ($n = 2$) while increasing the higher n -domain formation ($n = 3, 4$). In all films, the $n = 2$ domain shows a weak PB signature due to the overlapping negative photoinduced absorption band at the same energy, which possibly results from filling of higher n -domains as well as an ultrafast funneling toward higher n -domains.³⁹ This process is evident from the $n = 2$ and 3 n -domains decaying and the $n = 4$ n -domain showing a simultaneous growth at later delay times (10–100 ps). Energy transfer from lower n -domains to higher n -domains can also be observed from the decay of TA kinetics at $n = 3$ (460 nm) and a rise at $n = 4$ (480 nm) (Figure 2d–f). By analyzing the TA signal rise times for the $n = 4$ n -domain, we found the presence of an additional second growth rise-time (τ_2) in the OPA-treated samples, as opposed to a decay (τ_3) in the reference sample, which also signifies an efficient funneling into the higher n -domain (Table S1). Hence, steady-state absorbance, PL, and TA measurements confirm that OPA treatment

induces the growth of higher n -domains and lowers the formation of lower n -domains.

The possibility of OPA interaction with $\text{PBA}_2\text{Cs}_{n-1}\text{Pb}_n\text{Br}_{3n+1}$ films was confirmed by X-ray photon-spectroscopy (XPS) and Fourier-transform infrared spectroscopy (FTIR) measurement as shown in Figure 3a–c and Figure S3–S5, respectively. The presence of OPA in the final films was confirmed by the existence of P 2p spectra and significant gain in O 1s after OPA treatment. Traces of oxygen in ref sample is associated with organic surface contamination upon moisture exposure. Furthermore, upon OPA treatment, Pb 4f spectra slightly shifted toward lower binding energy, whereas no chemical peak shift was observed for Br 3d and Cs 3d of OPA-treated samples. This reveals that OPA binds with uncoordinated Pb^{2+} (as shown in the schematic in Figure 3d) on the surface and does not incorporate into the bulk. Simultaneously, surface treatment of $\text{PBA}_2\text{Cs}_{n-1}\text{Pb}_n\text{Br}_{3n+1}$ films with toluene containing OPA reduces the photoelectron intensity originating from perovskite phases (Pb 4f, Br 3d, Cs 3d, C 1s, and N 1s as shown in Table S2), suggesting the presence of a thin layer of OPA on the surface of the perovskite. However, this layer is discontinuous, or it is an ultrathin layer with slight nonuniformity, as revealed by XPS analysis of multiple spots on the sample (Figure S4). Moreover, the presence of OPA on the final solution was also confirmed by FTIR measurement of the films (Figure S5). As a control, the IR signature of P–O bond stretching vibration located at 1067 cm^{-1} is observed for OPA alone, which matches the value reported earlier.³⁶ The presence of the P–O bond stretching vibration peak in OPA-treated perovskite indicates successful incorporation of OPA in the film. The P–O bond stretching vibration peak shifted to 1071 cm^{-1} in OPA-treated perovskite, indicating that the P–O

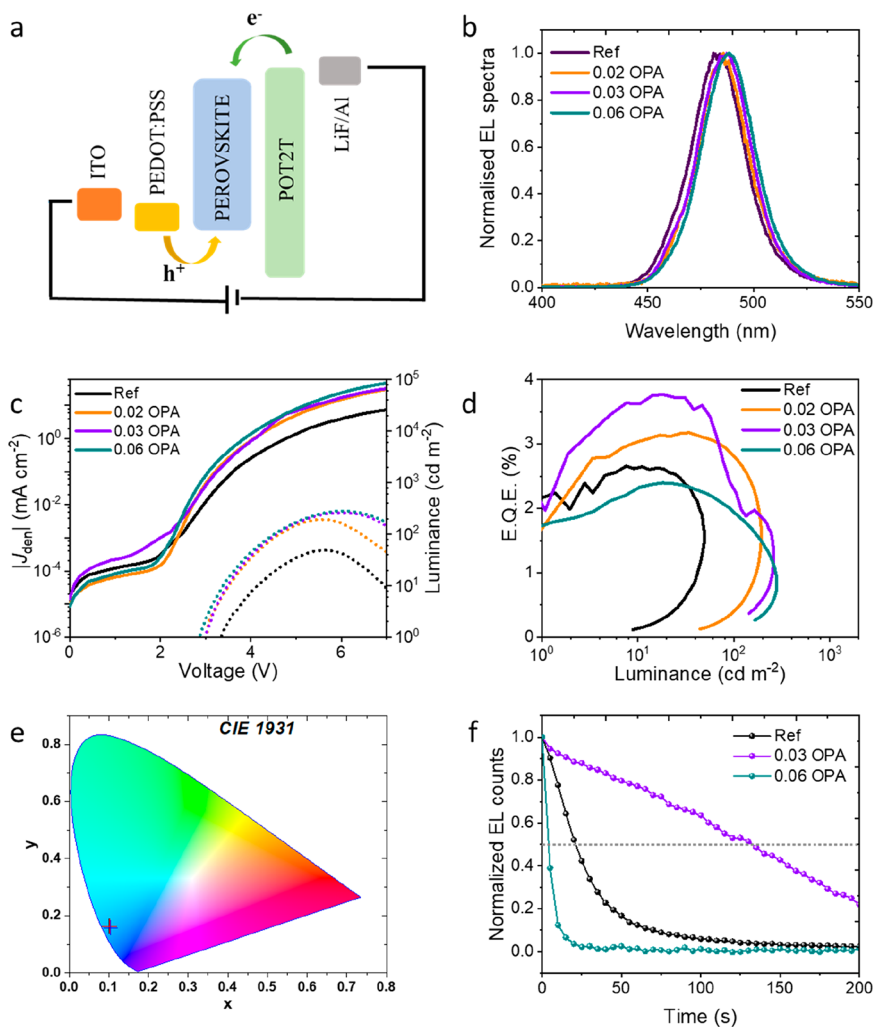


Figure 4. Device architecture of (a) PeLED, followed by the (b) electroluminescence spectra, (c) current density and luminance versus voltage, (d) external quantum efficiency, (e) CIE coordinates of the devices, and (f) operational stability of devices with and without OPA treatment.

265 bond is stretched possibly because of the bond formation
266 between OPA and the perovskite.

267 The surface morphology evolution of samples without and
268 with OPA treatment was monitored by using the scanning
269 electron microscopy technique (Figure S6). Compact films
270 were observed for both the control and OPA-treated samples.
271 The cross-sectional images of films without and with OPA
272 treatment indicates minimum changes on the film thickness
273 upon OPA treatment (Figure S7). Furthermore, XRD
274 measurements conducted on the control and OPA-treated
275 perovskite films (Figure S8) indicate an intensity enhancement
276 and a shift toward a lower angle for the peak at 11.68° , which
277 signifies better crystallinity and the growth of a domain with
278 bigger crystal structure upon OPA treatment.

279 To explore the change in the crystallization of perovskite
280 upon OPA addition, we performed liquid NMR spectroscopy
281 of OPA with perovskite precursors (Figure S9). $^{31}\text{P}\{^1\text{H}\}$ NMR
282 spectroscopy of pristine OPA is showing a chemical shift of
283 27.282 ppm, which subsequently shifted upfield upon the
284 introduction of PBABr (26.56 ppm), PbBr_2 (26.545 ppm), and
285 CsBr (26.507 ppm). This shift can be ascribed to the
286 modification in the chemical environment surrounding the
287 phosphorus nuclei in OPA, which originated from the
288 coordinative bonding between the P–OH or P=O functional

289 groups with Cs^+ , Pb^+ , and PBA^+ ions. Interestingly, such an
290 observation is unlike our previous investigation on TPPO,²⁵
291 where a downfield shifting has been observed. This could be
292 attributed to the presence of both P=O and P–O groups in
293 the OPA molecule, providing not only an inductive effect but
294 also a resonance effect that eventually results in a higher
295 shielding effect surrounding the P atom^{40,41} when coordinative
296 bonding happens with the Lewis acidic Cs^+ , Pb^{2+} , and PBA^+
297 ions. Strong molecular interaction between OPA and the PBA^+
298 ion as compared to the rest of the precursors ions could
299 decrease the probability of lower *n*-domain formation and
300 promote the formation of higher *n*-domains, in line with the
301 absorption, photoluminescence, and TA data.

302 The effect of radiative recombination upon OPA treatment
303 can be clearly observed in the photoluminescence quantum
304 yield (PLQY) data (Figure S1). Upon OPA treatment, the
305 PLQY of the samples increased compared to that of the
306 control (7.3%). The maximum PLQY was found on samples
307 with 0.03 mg/mL OPA treatment (53.2%). The enhanced
308 PLQY upon OPA treatment can be attributed to either lower
309 nonradiative recombination centers and/or better domains
310 distribution where acceptor (domains with lower bandgap) to
311 donor (domains with higher bandgap) ratio is balanced and
312 therefore promotes efficient carrier funneling.^{42,43}

The lower nonradiative recombination centers with OPA treatment are further confirmed by both time-resolved PL (TRPL) and space charge limited current (SCLC) measurement. Higher radiative lifetimes are observed on films upon OPA treatment (Figure S10 and Table S3). The luminescence decay is fitted by two lifetimes, i.e., τ_1 and τ_2 . The faster τ_1 corresponds to the recombination of free excitons in the RP samples. This is consistent with dynamics observed in our TA measurements (the same order of magnitude as τ_3 obtained from the TA dynamic of the $n = 4$ domain) and also from previous reports on RP systems.^{44,45} The smaller contribution to the PL comes from the slower component τ_2 , which is attributed to the defect-associated recombination. Upon treatment with OPA, we observed an enhancement of the lifetimes τ_1 and τ_2 on OPA-treated samples compared to the control sample. We also observed a lower contribution from defect-associated recombination to the radiative decay (decreasing A2), whereas the contribution of the free exciton recombination (A1) remains relatively constant. This unambiguously shows the suppression of defect-associated recombination due to passivation, enhancing the free exciton recombination in the OPA-treated films.

Moreover, to determine the density of defects in the control and OPA-treated samples, we performed space-charge-limited current (SCLC) measurement on the electron-only devices (Figure S11) that indicate a shift in the voltage at which the current changes from the ohmic ($J \sim V$) to the trap-filled limited ($J \sim V^x$, where $x > 2$) region from 0.95 to 0.76 V for the control and 0.03 OPA, respectively. This indicates a reduction in the total defect densities of OPA-treated samples from $3.4 \times 10^{18}/\text{cm}^3$ to $2.7 \times 10^{18}/\text{cm}^3$.

To explore the effect of OPA treatment on the devices, we fabricated PeLEDs by employing PEDOT: PSS and POT2T as the hole transport layer (HTL) and the electron transport layer (ETL), respectively (Figure 4a). The energy band level diagram of PeLEDs, drawn with values obtained from the literature,^{14,37} indicates the competence of electron and holes injection into the perovskite emissive layer. Although similar PL was observed, a red shift in the electroluminescence (EL) spectra (Figure 4b) of the devices was observed on the OPA-treated devices as compared to the control sample. This is in line with TA data, where higher n -domains are produced upon OPA treatment. The current density (J) and luminance (L) response of the devices versus voltage (V) is shown in Figure 4c, and device parameters are tabulated in Table 1. Overall,

treatment (Figure S11). In addition, a small shift in the ionization potential of samples upon OPA treatment were observed in photoelectron spectroscopy in air (PESA) data from 5.6 eV (for control) to 5.5 eV (for 0.03 OPA) (Figure S12), which may promote better carrier (especially hole) injection.

The highest EQE was found on devices with 0.03 OPA treatment. Figure 4d shows that the EQE of the control sample was 2.6%, whereas the EQE of the device with 0.03 OPA is enhanced up to 3.7%. This is in agreement with PLQY and PL measurement, where the highest PLQY can be found at 0.03 OPA. As both XPS and FTIR reveal the bond formation of OPA with uncoordinated Pb^{2+} , the low V_{th} and high EQE of OPA-treated samples indicates successful OPA passivation in the final thin film.

Figure 4e shows the color coordinate of the emission, whereas Figure 4f shows the operational stability of the device. The half-life (T_{50}) of the control device, which is when the device EL counts goes down to half of the initial value, found to be 20 s, and it increases up to 130 s for 0.03 mg/mL of OPA treatment. The evolution of electroluminescence spectra versus time (Figure S13) indicates that all devices exhibit spectral stability due to the use of a single halide system. The broadening of EL spectra at higher voltages (Figure S14) toward lower wavelength region can be attributed to the overfilling effect of the higher n -domain at higher carrier density.⁴³ The lifetime enhancement with OPA treatment could be due to the consequence of defect passivation in the device.

CONCLUSIONS

In conclusion, we found that the efficiency of blue emissive PeLEDs made with thin-film $\text{PBA}_2\text{Cs}_{n-1}\text{Pb}_n\text{Br}_{3n+1}$ is enhanced up to 3.7% upon increasing the OPA concentration (up to 0.03 mg/mL). The efficiency enhancement was enabled by both defect passivation and the crystallization modification done upon OPA treatment. Steady-state absorbance, PL, and TA reveal that OPA treatment reduces the lower n -domains and promotes the formation of higher n -domains. TA reveals that higher domains amplify after OPA treatment, confirming improved energy funneling from lower to higher n . Liquid NMR spectroscopy reveals the tendency to form higher n -domains is attributed to the strong OPA and PBA^{2+} ion interaction. From XPS spectra, the presence of OPA has been confirmed, which increases the passivation by making a bond with uncoordinated Pb^{2+} atoms. This is further confirmed by FTIR. Evidently, the perovskite films are passivated, and this is consequently shown by the enhancement of PLQY, which is a measure of radiative recombination in the film. The passivation effect was further supported by the reduction of defect densities after OPA addition measured by both SCLC and TRPL. The enhanced radiative recombination, therefore, enhances both the EQE and lifetime of the blue-emissive PeLEDs. Compact and uniform films were found even after OPA treatment. The successful incorporation of OPA in the thin film fabrication methods to passivate defects and increase the high n -domain formation are promising, as it can be translated to enhance the performance of other optoelectronic devices such as PeLEDs and photovoltaics.

ASSOCIATED CONTENT

Supporting Information

The Supporting Information is available free of charge at <https://pubs.acs.org/doi/10.1021/acsami.2c00899>.

Table 1. Detailed Device Parameters Based on OPA-CsPbBr₃

sample	EQE (%)	V_{th} (V)	current efficiency (Cd/A)	L_{max} (Cd/m ²)
ref	2.6 ± 0.3	3.3 ± 0.2	2.67	157.36
0.02	3.1 ± 0.3	2.8 ± 0.2	4.0	201.21
0.03	3.7 ± 0.3	3 ± 0.2	4.82	260.46
0.06	2.4 ± 0.3	2.9 ± 0.2	3.43	280.64

OPA-treated samples possess higher J and L , whereas the turn-on voltages (V_{th}) of the devices were lowered with OPA treatment. The lower V_{th} of the devices with OPA treatment were attributed to the better carrier injection because of (1) better energy alignment as well as (2) lower defects in the devices. SCLC measurement confirms the higher electron injection as well as lower defects densities upon OPA

426 (PDF)

<https://pubs.acs.org/10.1021/acsami.2c00899>

486

427 ■ AUTHOR INFORMATION

428 Corresponding Authors

429 **Natalia Yantara** – Energy Research Institute @ NTU (ERI@
430 N), Nanyang Technological University, Singapore 637553,
431 Singapore; orcid.org/0000-0003-3648-867X;

432 Email: nyantara@ntu.edu.sg

433 **Nripan Mathews** – Energy Research Institute @ NTU (ERI@
434 N), Nanyang Technological University, Singapore 637553,
435 Singapore; School of Materials Science and Engineering,
436 Nanyang Technological University, Singapore 639798,
437 Singapore; orcid.org/0000-0001-5234-0822;

438 Email: nripan@ntu.edu.sg

439 Authors

440 **Jayanta Kumar Mishra** – Energy Research Institute @ NTU
441 (ERI@N), Nanyang Technological University, Singapore
442 637553, Singapore; School of Materials Science and
443 Engineering, Nanyang Technological University, Singapore
444 639798, Singapore

445 **Anil Kanwat** – Energy Research Institute @ NTU (ERI@N),
446 Nanyang Technological University, Singapore 637553,
447 Singapore; orcid.org/0000-0002-5782-6909

448 **Tomoki Furuhashi** – School of Physical and Mathematical
449 Sciences, Nanyang Technological University, Singapore
450 637371, Singapore

451 **Sankaran Ramesh** – School of Physical and Mathematical
452 Sciences, Nanyang Technological University, Singapore
453 637371, Singapore; Energy Research Institute @NTU
454 (ERI@N), Interdisciplinary Graduate Programme, Nanyang
455 Technological University, Singapore 639798, Singapore;
456 orcid.org/0000-0002-1557-3798

457 **Teddy Salim** – School of Materials Science and Engineering,
458 Nanyang Technological University, Singapore 639798,
459 Singapore

460 **Nur Fadilah Jamaludin** – Energy Research Institute @ NTU
461 (ERI@N), Nanyang Technological University, Singapore
462 637553, Singapore

463 **Benny Febriansyah** – Energy Research Institute @ NTU
464 (ERI@N), Nanyang Technological University, Singapore
465 637553, Singapore; Berkeley Educational Alliance for
466 Research in Singapore (BEARS), Ltd., Singapore 138602,
467 Singapore

468 **Zi En Ooi** – Institute of Materials Research & Engineering,
469 Agency for Science, Technology and Research (A* STAR),
470 Singapore 138632, Singapore; orcid.org/0000-0001-9533-6655

472 **Subodh Mhaisalkar** – Energy Research Institute @ NTU
473 (ERI@N), Nanyang Technological University, Singapore
474 637553, Singapore; School of Materials Science and
475 Engineering, Nanyang Technological University, Singapore
476 639798, Singapore; orcid.org/0000-0002-9895-2426

477 **Tze Chien Sum** – School of Physical and Mathematical
478 Sciences, Nanyang Technological University, Singapore
479 637371, Singapore; orcid.org/0000-0003-4049-2719

480 **Kedar Hippalgaonkar** – School of Materials Science and
481 Engineering, Nanyang Technological University, Singapore
482 639798, Singapore; Institute of Materials Research &
483 Engineering, Agency for Science, Technology and Research
484 (A* STAR), Singapore 138632, Singapore

485 Complete contact information is available at:

Notes

The authors declare no competing financial interest.

■ ACKNOWLEDGMENTS

This research was funded by National Research Foundation (NRF), Prime Minister's Office, Singapore under its Competitive Research Programme (CRP Award NRF-CRP14-2014-03) and Ministry of Education, Singapore (MOE2019-T2-2-097). The photophysics studies were supported by the grants funded by the Singapore Ministry of Education under its AcRF Tier 2 grant (MOE-T2EP50120-0004) and the NRF under NRF Investigatorship (NRF-NRFI-2018-04).

■ REFERENCES

- (1) Dong, Q.; Lei, L.; Mendes, J.; So, F. Operational Stability of 500 Perovskite Light Emitting Diodes. *Journal of Physics: Materials* **2020**, *3* (1), 012002. 501
- (2) Zhang, L.; Sun, C.; He, T.; Jiang, Y.; Wei, J.; Huang, Y.; Yuan, M. High-Performance Quasi-2D Perovskite Light-Emitting Diodes: 504 from Materials to Devices. *Light: Science & Applications* **2021**, *10* (1), 61. 506
- (3) Xing, G.; Mathews, N.; Lim, S. S.; Yantara, N.; Liu, X.; Sabba, D.; Grätzel, M.; Mhaisalkar, S.; Sum, T. C. Low-Temperature Solution-Processed Wavelength-Tunable Perovskites for Lasing. *Nat. Mater.* **2014**, *13* (5), 476–480. 510
- (4) Heo, J. H.; Park, J. K.; Im, S. H. Full-Color Spectrum Coverage by High-Color-Purity Perovskite Nanocrystal Light-Emitting Diodes. *Cell Reports Physical Science* **2020**, *1* (9), 100177. 513
- (5) Si, J.; Liu, Y.; He, Z.; Du, H.; Du, K.; Chen, D.; Li, J.; Xu, M.; Tian, H.; He, H.; Di, D.; Lin, C.; Cheng, Y.; Wang, J.; Jin, Y. Efficient and High-Color-Purity Light-Emitting Diodes Based on In Situ Grown Films of CsPbX₃ (X = Br, I) Nanoplates with Controlled Thicknesses. *ACS Nano* **2017**, *11* (11), 11100–11107. 518
- (6) Protesescu, L.; Yakunin, S.; Bodnarchuk, M. I.; Krieg, F.; Caputo, R.; Hendon, C. H.; Yang, R. X.; Walsh, A.; Kovalenko, M. V. Nanocrystals of Cesium Lead Halide Perovskites (CsPbX₃, X = Cl, Br, and I): Novel Optoelectronic Materials Showing Bright Emission with Wide Color Gamut. *Nano Lett.* **2015**, *15* (6), 3692–3696. 523
- (7) Miyata, A.; Mitoglu, A.; Plochocka, P.; Portugall, O.; Wang, J. T.-W.; Stranks, S. D.; Snaith, H. J.; Nicholas, R. J. Direct Measurement of the Exciton Binding Energy and Effective Masses for Charge Carriers in Organic–Inorganic Tri-Halide Perovskites. *Nat. Phys.* **2015**, *11* (7), 582–587. 528
- (8) Chen, B.; Yang, M.; Priya, S.; Zhu, K. Origin of J–V Hysteresis in Perovskite Solar Cells. *J. Phys. Chem. Lett.* **2016**, *7* (5), 905–917. 530
- (9) Wang, F.; Bai, S.; Tress, W.; Hagfeldt, A.; Gao, F. Defects Engineering for High-Performance Perovskite Solar Cells. *npj Flexible Electronics* **2018**, *2* (1), 22. 533
- (10) Cao, Y.; Wang, N.; Tian, H.; Guo, J.; Wei, Y.; Chen, H.; Miao, Y.; Zou, W.; Pan, K.; He, Y.; Cao, H.; Ke, Y.; Xu, M.; Wang, Y.; Yang, M.; Du, K.; Fu, Z.; Kong, D.; Dai, D.; Jin, Y.; Li, G.; Li, H.; Peng, Q.; Wang, J.; Huang, W. Perovskite Light-Emitting Diodes Based on Spontaneously Formed Submicrometre-Scale Structures. *Nature* **2018**, *562* (7726), 249–253. 539
- (11) Chiba, T.; Hayashi, Y.; Ebe, H.; Hoshi, K.; Sato, J.; Sato, S.; Pu, Y.-J.; Ohisa, S.; Kido, J. Anion-Exchange Red Perovskite Quantum Dots with Ammonium Iodine Salts for Highly Efficient Light-Emitting Devices. *Nat. Photonics* **2018**, *12* (11), 681–687. 543
- (12) Vashishtha, P.; Halpert, J. E. Field-Driven Ion Migration and Color Instability in Red-Emitting Mixed Halide Perovskite Nanocrystal Light-Emitting Diodes. *Chem. Mater.* **2017**, *29* (14), 5965–5973. 547

- 548 (13) Haruyama, J.; Sodeyama, K.; Han, L.; Tateyama, Y.
549 Termination Dependence of Tetragonal CH₃NH₃PbI₃ Surfaces for
550 Perovskite Solar Cells. *J. Phys. Chem. Lett.* **2014**, *5* (16), 2903–2909.
- 551 (14) Kanwat, A.; Yantara, N.; Ng, Y. F.; Hooper, T. J. N.; Rana, P. J.
552 S.; Febriansyah, B.; Harikesh, P. C.; Salim, T.; Vashishtha, P.;
553 Mhaisalkar, S. G.; Mathews, N. Stabilizing the Electroluminescence of
554 Halide Perovskites with Potassium Passivation. *ACS Energy Lett.*
555 **2020**, *5* (6), 1804–1813.
- 556 (15) Zirak, M.; Moya, E.; Alehdaghi, H.; Kanwat, A.; Choi, W.-C.;
557 Jang, J. Anion- and Cation-Codoped All-Inorganic Blue-Emitting
558 Perovskite Quantum Dots for Light-Emitting Diodes. *ACS Applied*
559 *Nano Materials* **2019**, *2* (9), S655–S662.
- 560 (16) Kanwat, A.; Moya, E.; Cho, S.; Jang, J. Rubidium as an
561 Alternative Cation for Efficient Perovskite Light-Emitting Diodes.
562 *ACS Appl. Mater. Interfaces* **2018**, *10* (19), 16852–16860.
- 563 (17) Karlsson, M.; Yi, Z.; Reichert, S.; Luo, X.; Lin, W.; Zhang, Z.;
564 Bao, C.; Zhang, R.; Bai, S.; Zheng, G.; et al. Mixed Halide Perovskites
565 for Spectrally Stable and High-Efficiency Blue Light-Emitting Diodes.
566 *Nat. Commun.* **2021**, *12* (1), 361.
- 567 (18) Na Quan, L.; Ma, D.; Zhao, Y.; Voznyy, O.; Yuan, H.; Bladt, E.;
568 Pan, J.; García de Arquer, F. P.; Sabatini, R.; Piontkowski, Z.; et al.
569 Edge Stabilization in Reduced-Dimensional Perovskites. *Nat.*
570 *Commun.* **2020**, *11* (1), 170.
- 571 (19) Yang, X.; Zhang, X.; Deng, J.; Chu, Z.; Jiang, Q.; Meng, J.;
572 Wang, P.; Zhang, L.; Yin, Z.; You, J. Efficient Green Light-Emitting
573 Diodes Based on Quasi-Two-Dimensional Composition and Phase
574 Engineered Perovskite with Surface Passivation. *Nat. Commun.* **2018**,
575 *9* (1), 570.
- 576 (20) Kim, D. H.; Muzzillo, C. P.; Tong, J.; Palmstrom, A. F.; Larson,
577 B. W.; Choi, C.; Harvey, S. P.; Glynn, S.; Whitaker, J. B.; Zhang, F.;
578 Li, Z.; Lu, H.; van Hest, M. F. A. M.; Berry, J. J.; Mansfield, L. M.;
579 Huang, Y.; Yan, Y.; Zhu, K. Bimolecular Additives Improve Wide-
580 Band-Gap Perovskites for Efficient Tandem Solar Cells with CIGS.
581 *Joule* **2019**, *3* (7), 1734–1745.
- 582 (21) Wang, H.; Zhang, X.; Wu, Q.; Cao, F.; Yang, D.; Shang, Y.;
583 Ning, Z.; Zhang, W.; Zheng, W.; Yan, Y.; et al. Trifluoroacetate
584 Induced Small-Grained CsPbBr₃ Perovskite Films Result in Efficient
585 and Stable Light-Emitting Devices. *Nat. Commun.* **2019**, *10* (1), 665.
- 586 (22) Fang, Z.; Chen, W.; Shi, Y.; Zhao, J.; Chu, S.; Zhang, J.; Xiao,
587 Z. Dual Passivation of Perovskite Defects for Light-Emitting Diodes
588 with External Quantum Efficiency Exceeding 20%. *Adv. Funct. Mater.*
589 **2020**, *30* (12), 1909754.
- 590 (23) Xu, W.; Hu, Q.; Bai, S.; Bao, C.; Miao, Y.; Yuan, Z.; Borzda, T.;
591 Barker, A. J.; Tyukalova, E.; Hu, Z.; Kaweck, M.; Wang, H.; Yan, Z.;
592 Liu, X.; Shi, X.; Uvdal, K.; Fahlman, M.; Zhang, W.; Duchamp, M.;
593 Liu, J.-M.; Petrozza, A.; Wang, J.; Liu, L.-M.; Huang, W.; Gao, F.
594 Rational Molecular Passivation for High-Performance Perovskite
595 Light-Emitting Diodes. *Nat. Photonics* **2019**, *13* (6), 418–424.
- 596 (24) Xu, L.; Li, J.; Cai, B.; Song, J.; Zhang, F.; Fang, T.; Zeng, H. A
597 Bilateral Interfacial Passivation Strategy Promoting Efficiency and
598 Stability of Perovskite Quantum Dot Light-Emitting Diodes. *Nat.*
599 *Commun.* **2020**, *11* (1), 3902.
- 600 (25) Jamaludin, N. F.; Yantara, N.; Febriansyah, B.; Tay, Y. B.;
601 Muhammad, B. T.; Laxmi, S.; Lim, S. S.; Sum, T. C.; Mhaisalkar, S.;
602 Mathews, N. Additives in Halide Perovskite for Blue-Light-Emitting
603 Diodes: Passivating Agents or Crystallization Modulators? *ACS Energy*
604 *Lett.* **2021**, *6* (12), 4265–4272.
- 605 (26) Xing, G.; Wu, B.; Wu, X.; Li, M.; Du, B.; Wei, Q.; Guo, J.;
606 Yeow, E. K. L.; Sum, T. C.; Huang, W. Transcending the Slow
607 Bimolecular Recombination in Lead-Halide Perovskites for Electro-
608 luminescence. *Nat. Commun.* **2017**, *8* (1), 14558.
- 609 (27) Pang, P.; Jin, G.; Liang, C.; Wang, B.; Xiang, W.; Zhang, D.; Xu,
610 J.; Hong, W.; Xiao, W.; Zhang, L.; Xing, G.; Chen, J.; Ma, D.
611 Rearranging Low-Dimensional Phase Distribution of Quasi-2D
612 Perovskites for Efficient Sky-Blue Perovskite Light-Emitting Diodes.
613 *ACS Nano* **2020**, *14* (9), 11420–11430.
- 614 (28) Nenon, D. P.; Pressler, K.; Kang, J.; Koscher, B. A.; Olshansky,
615 J. H.; Osowiecki, W. T.; Koc, M. A.; Wang, L.-W.; Alivisatos, A. P.
616 Design Principles for Trap-Free CsPbX₃ Nanocrystals: Enumerating
and Eliminating Surface Halide Vacancies with Softer Lewis Bases. *J.*
Am. Chem. Soc. **2018**, *140* (50), 17760–17772.
- (29) Smock, S. R.; Williams, T. J.; Brutchey, R. L. Quantifying the
Thermodynamics of Ligand Binding to CsPbBr₃ Quantum Dots. *Angew.*
Chem., Int. Ed. **2018**, *57* (36), 11711–11715.
- (30) Brown, A. A. M.; Hooper, T. J. N.; Veldhuis, S. A.; Chin, X. Y.;
Bruno, A.; Vashishtha, P.; Tey, J. N.; Jiang, L.; Damodaran, B.; Pu, S.
H.; Mhaisalkar, S. G.; Mathews, N. Self-Assembly of a Robust
Hydrogen-Bonded Octylphosphonate Network on Cesium Lead
Bromide Perovskite Nanocrystals for Light-Emitting Diodes. *Nano-*
scale **2019**, *11* (25), 12370–12380.
- (31) Tan, Y.; Zou, Y.; Wu, L.; Huang, Q.; Yang, D.; Chen, M.; Ban,
M.; Wu, C.; Wu, T.; Bai, S.; Song, T.; Zhang, Q.; Sun, B. Highly
Luminescent and Stable Perovskite Nanocrystals with Octylphos-
phonic Acid as a Ligand for Efficient Light-Emitting Diodes. *ACS*
Appl. Mater. Interfaces **2018**, *10* (4), 3784–3792.
- (32) Xiao, P.; Yu, Y.; Cheng, J.; Chen, Y.; Yuan, S.; Chen, J.; Yuan,
J.; Liu, B. Advances in Perovskite Light-Emitting Diodes Possessing
Improved Lifetime. *Nanomaterials* **2021**, *11* (1), 103.
- (33) Cho, H.; Kim, J. S.; Wolf, C.; Kim, Y. H.; Yun, H. J.; Jeong, S.
H.; Sadhanala, A.; Venugopalan, V.; Choi, J. W.; Lee, C. L.; Friend, R.
H.; Lee, T. W. High-Efficiency Polycrystalline Perovskite Light-
Emitting Diodes Based on Mixed Cations. *ACS Nano* **2018**, *12* (3),
2883–2892.
- (34) McGrath, F.; Ghorpade, U. V.; Ryan, K. M. Synthesis and
Dimensional Control of CsPbBr₃ Perovskite Nanocrystals using
Phosphorous Based Ligands. *J. Chem. Phys.* **2020**, *152* (17), 174702.
- (35) Tan, Y.; Zou, Y.; Wu, L.; Huang, Q.; Yang, D.; Chen, M.; Ban,
M.; Wu, C.; Wu, T.; Bai, S.; Song, T.; Zhang, Q.; Sun, B. Highly
Luminescent and Stable Perovskite Nanocrystals with Octylphos-
phonic Acid as a Ligand for Efficient Light-Emitting Diodes. *ACS*
Appl. Mater. Interfaces **2018**, *10* (4), 3784–3792.
- (36) Wu, Y.; Liu, L.; Wang, W.; Zhang, W.; Yu, H.; Qian, J.; Chen,
Y.; Shen, W.; Sui, S.; Deng, Z.; Chen, S.; Huang, W. Enhanced
Stability and Performance of Light-Emitting Diodes Based on In Situ
Fabricated FAPbBr₃ Nanocrystals via Ligand Compensation with n-
Octylphosphonic Acid. *Journal of Materials Chemistry C* **2020**, *8* (29),
9936–9944.
- (37) Yantara, N.; Bruno, A.; Iqbal, A.; Jamaludin, N. F.; Soci, C.;
Mhaisalkar, S.; Mathews, N. Designing Efficient Energy Funneling
Kinetics in Ruddlesden-Popper Perovskites for High-Performance
Light-Emitting Diodes. *Adv. Mater.* **2018**, *30*, e1800818.
- (38) Ng, Y. F.; Kulkarni, S. A.; Parida, S.; Jamaludin, N. F.; Yantara,
N.; Bruno, A.; Soci, C.; Mhaisalkar, S.; Mathews, N. Highly Efficient
Cs-based Perovskite Light-Emitting Diodes Enabled by Energy
Funnelling. *Chem. Commun. (Camb)* **2017**, *53* (88), 12004–12007.
- (39) Giovanni, D.; Ramesh, S.; Righetto, M.; Melvin Lim, J. W.;
Zhang, Q.; Wang, Y.; Ye, S.; Xu, Q.; Mathews, N.; Sum, T. C. The
Physics of Interlayer Exciton Delocalization in Ruddlesden–Popper
Lead Halide Perovskites. *Nano Lett.* **2021**, *21* (1), 405–413.
- (40) Mulloyarova, V. V.; Giba, I. S.; Kostin, M. A.; Denisov, G. S.;
Shenderovich, I. G.; Tolstoy, P. M. Cyclic Trimers of Phosphinic
Acids in Polar Aprotic Solvent: Symmetry, Chirality and H/D Isotope
Effects on NMR Chemical Shifts. *Phys. Chem. Chem. Phys.* **2018**, *20*
(7), 4901–4910.
- (41) Venkatramiah, N.; Mendes, R. F.; Silva, A. M. S.; Tome, J. P.
C.; Almeida Paz, F. A. A Ladder Coordination Polymer Based on
Ca²⁺ and (4,5-dicyano-1,2-phenylene)bis(phosphonic acid): Crystal
Structure and Solution-State NMR Study. *Acta Crystallographica*
Section C **2016**, *72* (9), 685–691.
- (42) Ng, Y. F.; Febriansyah, B.; Jamaludin, N. F.; Giovanni, D.;
Yantara, N.; Chin, X. Y.; Tay, Y. B.; Sum, T. C.; Mhaisalkar, S.;
Mathews, N. Design of 2D Templating Molecules for Mixed-
Dimensional Perovskite Light-Emitting Diodes. *Chem. Mater.* **2020**,
32 (19), 8097–8105.
- (43) Yantara, N.; Bruno, A.; Iqbal, A.; Jamaludin, N. F.; Soci, C.;
Mhaisalkar, S.; Mathews, N. Designing Efficient Energy Funneling
Kinetics in Ruddlesden–Popper Perovskites for High-Performance
Light-Emitting Diodes. *Adv. Mater.* **2018**, *30* (33), 1800818.

- 686 (44) Giovanni, D.; Chong, W. K.; Dewi, H. A.; Thirumal, K.; Neogi,
687 I.; Ramesh, R.; Mhaisalkar, S.; Mathews, N.; Sum, T. C. Tunable
688 Room-Temperature Spin-Selective Optical Stark Effect in Solution-
689 Processed Layered Halide Perovskites. *Science Advances* **2016**, *2* (6),
690 e1600477.
- 691 (45) Chong, W. K.; Thirumal, K.; Giovanni, D.; Goh, T. W.; Liu, X.;
692 Mathews, N.; Mhaisalkar, S.; Sum, T. C. Dominant Factors Limiting
693 the Optical Gain in Layered Two-Dimensional Halide Perovskite
694 Thin Films. *Phys. Chem. Chem. Phys.* **2016**, *18* (21), 14701–14708.